Array atomic force microscopy for real-time multiparametric analysis

Qingqing Yang[a,1], Qian Ma[b,1], Kate M. Herum[c,2], Chonghe Wang[d], Nirav Patel[c], Joon Lee[a,3], Shanshan Wang[e,f], Tony M. Yen[c], Jun Wang[c], Hanmei Tang[d], Yu-Hwa Lo[b], Brian P. Head[e,f], Farooq Azam[g], Sheng Xu[a,d], Gert Cauwenberghs[c], Andrew D. McCulloch[c,h], Scott John[i], Zhaowei Liu[a,b,4], and Ratnesh Lal[a,c,j,k,4]

[a]Materials Science and Engineering, University of California, San Diego, La Jolla, CA 92093; [b]Department of Electrical and Computer Engineering, University of California, San Diego, La Jolla, CA 92093; [c]Department of Bioengineering, University of California, San Diego, La Jolla, CA 92093; [d]Department of Nanoengineering, University of California, San Diego, La Jolla, CA 92093; [e]Department of Anesthesiology, University of California, San Diego, La Jolla, CA 92093; [f]Department of Anesthesia, Veterans Affairs San Diego Healthcare System, San Diego, CA 92161; [g]Marine Biology Research Division, Scripps Institution of Oceanography, University of California, San Diego, La Jolla, CA 92093; [h]Department of Medicine, University of California, San Diego, La Jolla, CA 92093; [i]Cardiovascular Research Laboratory, University of California, Los Angeles, CA 90095; [j]Department of Mechanical and Aerospace Engineering, University of California, San Diego, La Jolla, CA 92093; and [k]Institute of Engineering in Medicine, University of California, San Diego, La Jolla, CA 92093

Edited by David A. Weitz, Harvard University, Cambridge, MA, and approved February 11, 2019 (received for review August 6, 2018)

Nanoscale multipoint structure–function analysis is essential for deciphering the complexity of multiscale biological and physical systems. Atomic force microscopy (AFM) allows nanoscale structure–function imaging in various operating environments and can be integrated seamlessly with disparate probe-based sensing and manipulation technologies. Conventional AFMs only permit sequential single-point analysis; widespread adoption of array AFMs for simultaneous multipoint study is challenging owing to the intrinsic limitations of existing technological approaches. Here, we describe a prototype dispersive optics-based array AFM capable of simultaneously monitoring multiple probe–sample interactions. A single supercontinuum laser beam is utilized to spatially and spectrally map multiple cantilevers, to isolate and record beam deflection from individual cantilevers using distinct wavelength selection. This design provides a remarkably simplified yet effective solution to overcome the optical cross-talk while maintaining subnanometer sensitivity and compatibility with probe-based sensors. We demonstrate the versatility and robustness of our system on parallel multiparametric imaging at multiscale levels ranging from surface morphology to hydrophobicity and electric potential mapping in both air and liquid, mechanical wave propagation in polymeric films, and the dynamics of living cells. This multiparametric, multiscale approach provides opportunities for studying the emergent properties of atomic-scale mechanical and physicochemical interactions in a wide range of physical and biological networks.

atomic force microscopy | dispersive optics | multiparametric analysis | nanobiosensing | nanoimaging

Dynamic multiscale systems ranging from nanoheterostructured materials (1), surface and intersurface sciences (2), and intricate biological networks (3) to sensors and devices (4) have unique emergent properties owing to the complex coordination of structure and function among their constituent units. Our understanding of these multiscale interactions has been limited by the paucity of appropriate tools allowing real-time and simultaneous nanoscale structure–function investigation of multiple subcomponents in complex systems. Although common approaches, including multielectrode arrays (5), fluorescent indicators (6), ultrasound imaging (7), and magnetic resonance imaging (8) enable recording and tracking activities in situ, they have limited spatial resolution. High-resolution systems such as electron microscopy (EM) suffer from inability to study living material due to environmental constraints (9). In contrast, atomic force microscopy (AFM), without such severe environmental constraints, uses interactions between a nanoscale probe and the sample, allowing resolution that extends from micro to nano and subnano scales, enabling examination of objects such as nanoparticles, proteins, DNA, and even single molecules under physiological conditions (10–13). Additionally, functionalized AFM probes have been developed for quantitatively measuring various physicochemical properties including thermal energy (14), chemical force (15), conductance (16), and magnetism (17). The current AFM technology limits these multiparametric studies to single, one-time-point applications (18, 19). To overcome such limitations, array AFM platforms that can achieve high-resolution multipoint simultaneous imaging and mapping physicochemical properties are expected to have wide applicability in investigating the cooperative and coordinated activities of various biological and physical systems.

AFM works by measuring a cantilever deflection proportional to sample–probe interaction force. Among all of the available array

Significance

High-resolution multipoint simultaneous structure–function analysis is becoming of great interest in a broad spectrum of fields for deciphering multiscale dynamics, especially in biophysics and materials science. However, current techniques are limited in terms of versatility, resolution, throughput, and biocompatibility. Here, a multifunctional imaging platform is introduced that shows high sensitivity, minimum cross-talk, and a variety of probe-based sensing. This is demonstrated by parallel multiparametric studies in air and liquid, including mechanical wave propagation in a soft polymer film, imaging of live neurons, and cooperative activities of living coupled cardiac muscle cells. As an experimental demonstration of array atomic force microscopy for multiparametric analysis in dynamic systems this work sheds light on the study of emergent properties in wide-ranging fields.

Author contributions: Q.Y., Q.M., Z.L., and R.L. designed research; Q.Y., Q.M., K.M.H., C.W., N.P., J.L., S.W., T.M.Y., and J.W. performed research; Q.Y., Q.M., K.M.H., N.P., J.L., J.W., H.T., Y.-H.L., B.P.H., F.A., S.X., G.C., A.D.M., S.J., Z.L., and R.L. analyzed data; and Q.Y. wrote the paper.

Conflict of interest statement: A.D.M. is a cofounder of Insilicomed and Vektor Medical, and serves on the scientific advisory boards. He has an equity interest in Insilicomed. His research grants, including those acknowledged here, have been identified for conflict of interest management by the University of California, San Diego based on the overall scope of the research and its potential benefit to these entities. B.P.H. is scientific founder of CavoGene LifeSciences LLC and holds equity interest in the company.

This article is a PNAS Direct Submission.

[1]Q.Y. and Q.M. contributed equally to this work.

[2]Present address: Institute for Experimental Medical Research, Oslo University Hospital, Oslo 0450, Norway.

[3]Present address: Department of Biochemistry, Weill Cornell Medicine, New York, NY 10065.

[4]To whom correspondence may be addressed. Email: zhaowei@ucsd.edu or rlal@ucsd.edu.

This article contains supporting information online at www.pnas.org/lookup/suppl/doi:10.1073/pnas.1813518116/-/DCSupplemental.

Published online March 8, 2019.

AFM readout systems, optical beam deflection (OBD) is the most simple and robust method (20, 21). The main limitation of OBD is its difficulty to scale down to densely compacted cantilever arrays owing to optical cross-talk (22, 23), which is particularly important for short-range investigations as demonstrated in single-cell studies (24). One solution acts by combining expanded illumination laser beam with multifrequency cantilever actuation, thereby reducing optical cross-talk by driving each cantilever at different frequencies. This does, however, restrict the cantilever to work only in dynamic mode and cannot be used simultaneously with other AFM modalities (i.e., those requiring a firm tip–sample contact, such as the measurement of chemical forces and mechanical properties) (25). Another optical method, interferometric readout measuring the phase of deflected beam instead of angle, provides an alternative approach to overcome cross-talk, but it is complicated in setup, limited to small displacement of the cantilever, thus limiting its scalability, and also highly sensitive to environmental noise (26). Other than optical readouts, electronic readouts involving capacitance (27), piezoresistivity (28, 29), piezoelectricity (30), and metal-oxide semiconductor field effect (31) have also been used for cantilever array detection; they show progress but are limited by microfabrication complexity and lack biocompatibility.

To overcome these limitations, we have developed an advanced OBD readout method-based array AFM platform, called spectral-spatially encoded array AFM (SEA-AFM). This achieves simultaneous multipoint and multiparametric nanoscale analyses and, due to few environmental constraints, retains biological compatibility. A single supercontinuum laser beam and dispersive optical elements are utilized to spectrally and spatially map an array of cantilevers such that each cantilever has a unique wavelength channel associated with it. The deflected beams from multiple cantilevers can therefore be addressed both simultaneously and independently via wavelength selection. In this way, the detection system is significantly simplified and the cross-talk problem is overcome, all the while maintaining high sensitivity and scalability. To demonstrate the SEA-AFM platform's versatility and robustness we have applied our newly designed array to multiple physical and biological systems for simultaneous structure–function analysis.

Results and Discussion

System Design. The general design and working principle of the SEA-AFM are shown in Fig. 1 and *SI Appendix*, Figs. S1 and S2. The system consists of a supercontinuum laser with associated optics, a customized MultiMode AFM equipped with a Nanoscope controller III (Bruker) and quadrant photodetectors (QPDs). Broadband light beam from a supercontinuum laser is reflected by a dispersive grating and the stretched beam is projected onto an array of reflective cantilevers. An image of the projected spectrally gradient laser beam on a cantilever array is shown in *SI Appendix*, Fig. S1. Reflected beams of different wavelengths from multiple cantilevers are separated by an optical demultiplexing device, such as a series of dichroic beam splitters, and detected by an array of QPDs. Although in principle the SEA-AFM system can be adapted to different AFM modalities, AFM imaging in this study is done in constant height mode.

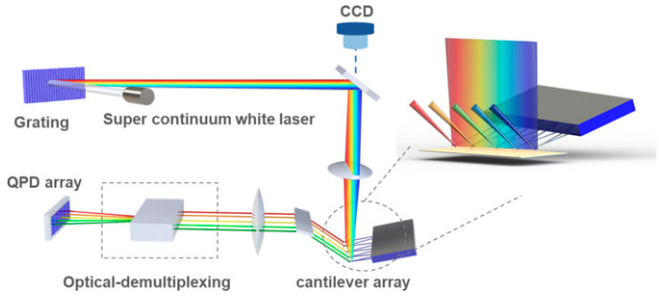

Fig. 1. SEA-AFM system. A supercontinuum laser, reflected by a grating (groove 300 mm^{-1}), transmits through a focusing lens and projects a spectral gradient onto a cantilever array. Each cantilever is illuminated by light with a distinct wavelength. The beams deflected by the array of cantilevers are monitored by a QPD array following an optical frequency demultiplexing component, such as a series of dichroic beam splitters and filters.

The dispersive optics-based readout method minimizes the cross-talk by assigning each cantilever an independent wavelength channel. A proof-of-concept test shows that two adjacent cantilevers can be individually illuminated and recorded by wavelength selection with the SEA-AFM approach (*SI Appendix*, Fig. S3). We vibrated the paired cantilever array using an external inertial drive, performed a frequency sweep from 0 to 100 kHz, and used a QPD to monitor beam reflections from the two cantilevers. For incident laser beams with wavelengths from 630 to 670 nm we measured two characteristic peaks corresponding to the resonance frequencies of the cantilevers; for a 640-nm (10-nm bandwidth) laser beam only a 23-kHz peak is observed, and for a 660-nm wavelength (10-nm bandwidth) only a 65-kHz peak is observed (*SI Appendix*, Fig. S3*A*).

Cross-talk between two cantilevers was minimized as determined by cantilever separation and the focal spot size at each wavelength channel. For the system shown in *SI Appendix*, Fig. S1*A* ~16-μm illumination spot size at a single wavelength channel determined the minimum separation of two cantilevers without obvious cross-talk. The "rainbow" beam that is projected on the cantilever array has a length of 1.2 mm, making it potentially suitable to illuminate up to ~70 cantilevers (16-μm separation) without significant cross-talk while not further complicating the illumination system (*SI Appendix*, section 1). By further optimizing the system (e.g., smaller illumination spot size and larger grating dispersion), the minimum space between two neighboring cantilevers could be more reduced. In practice, the geometry of the cantilever and the operational condition will also affect the number of cantilevers that can be packed in the system. Notably, this method can be adapted to illuminate a 2D AFM array with a larger number of tips via slight modification of the optics.

In general, optical readouts eliminate most of the electronic and thermal cross-talk that hinders the high-density array (32–34). As we mentioned earlier, single-frequency optical readouts are typically challenging for large-scale closely packed array AFM (22, 25). In the case of SEA-AFM, the spectral information represents an additional degree of freedom, leading to the cantilever packing density close to the optical diffraction limit without substantial cross-talk.

Since SEA-AFM has the same detection principle as conventional OBD (20), the theoretical limit of the detection sensitivity obtained by SEA-AFM should be almost identical to conventional OBD. We tested the noise power spectrum of our SEA-AFM using a silicon cantilever (Bruker MPP-21100, spring constant k = 3 N/m) (*SI Appendix*, section 2 and Figs. S4–S6). Through adjusting the laser power and optimizing the beam shape, the deflection noise density floor of our current setup reaches around 350 fm/$\sqrt{\text{Hz}}$. Importantly, most of the conventionally reported techniques which have been applied to improve the signal-to-noise ratio of the OBD method are equally well-suited to SEA-AFM (35–40). Thus, we speculate that by further optimizing the system the noise level of SEA-AFM will be close to that of commercially available AFMs.

Parallel Topography Imaging. We evaluated the feasibility of the array AFM system for parallel topography imaging. Two different areas on the calibration grating (Fig. 2*A*) were imaged simultaneously in constant height mode with our customized silicon nitride cantilever array (*SI Appendix*, Fig. S7; the two probes have similar cantilever length of ~200 μm with ~388 μm

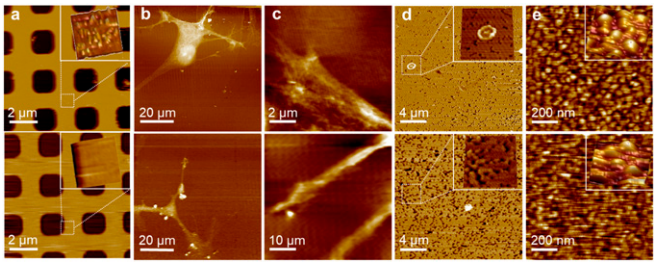

Fig. 2. Parallel SEA-AFM morphology imaging of various samples using double cantilevers. Top images are from cantilever 1, and bottom images are from cantilever 2. (*A*) Standard calibration grid (pitch size: 3 μm). Insets with relative same locations: 1 μm × 1 μm. (*B*) Fixed human differentiated neural progenitor cells (NPCs) derived from induced pluripotent stem cells in air. (*C*) Live NPCs in fluid. (*D*) Filtered seawater samples on 0.22-μm track-etched polycarbonate membranes with different types of captured particulate matter. Insets with relative same locations: 4 μm × 4 μm. (*E*) Sputtered gold nanoparticles (*Top Inset*, ~200 nm × 200 nm; *Bottom Inset*, 150 nm × 150 nm). Although great care was taken to engage both cantilevers at the same time, cantilever 2 in this example still has larger scanning force than cantilever 1, so the images taken by cantilever 2 show more streaky artifacts.

apart). Cross-talk between the two cantilevers is not observed. To further demonstrate the imaging capabilities and resolution of the array AFM under different environmental conditions, multiple samples were used: fixed and live human differentiated neural progenitor cells, filtered seawater samples, and sputtered gold nanoparticles (Fig. 2 *B*–*E*). These imaging measurements validated the applicability of the SEA-AFM system for the demanding parallel AFM topography imaging in both air and liquid. A promising solution for further improvement is to adapt reported active probe array (34, 41) in our SEA-AFM to achieve independent force control of each cantilever.

Parallel Structure–Function Mapping. A major advantage of the SEA-AFM is its compatibility to varied probe-based sensors for multifunctional imaging thanks to the simplicity and sensitivity of the optical lever readout mode. As an example, we chemically functionalized SiNx AFM tips (Fig. 3*A*) with a CH_3-terminated monolayer of octadecyltrichlorosilane (OTS), yielding a hydrophobic surface that can discern hydrophilic and hydrophobic areas by adhesion force measurements. Fig. 3*B* shows the schematics and optical image of the sample: the hydrophobic fluoropolymer Cytop was patterned onto a hydrophilic SiO_2 glass slide. Morphology and hydrophobicity maps were imaged in deionized water (42). We took simultaneous AFM images in constant height mode on two sample areas (Fig. 3 *C* and *D*), which are outlined in Fig. 3*B*. The areas were investigated by force mapping to measure the adhesion forces with the functionalized tips. The simultaneous force mapping of the two areas is shown in Fig. 3 *E* and *F*. Each pixel of the adhesion maps gives the absolute value of the peak height (attractive forces are negative). In the two resulting adhesion maps, larger adhesion forces were detected on the Cytop patterns, the hydrophobic areas terminated with CF_2 groups; smaller adhesion forces were found on the hydrophilic SiO_2 areas with silanol Si–OH groups on the surface. Six groups of typical retraction force-distance curves are plotted in Fig. 3 *G* and *H*, with corresponding pixels marked on the adhesion maps with the same colors as the force curves. Quantitatively, the attraction force on the hydrophobic area is approximately nine times larger than the force recorded from the hydrophilic area.

Simultaneous multipoint structure-hydrophobic mapping is a useful tool to better understand biological processes (43). Moreover, the applicability of the functionalized probe is not limited to structure-hydrophobic mapping and could be extended to other probe sensors, such as thermal, chemical, pH, and so on. For more examples, we have explored the feasibility of using conductive parallel AFM to simultaneously detect surface morphology and electric potential (*SI Appendix*, section 3 and Fig. S9). Together, these measurements highlight the multiparametric characterization capabilities of the SEA-AFM.

Detection of Mechanical Wave Propagation on Soft Polymer Film. In addition to mapping topography and chemical forces of static samples, we examined the applicability of the AFM array in a dynamic system: an ultrasensitive detection of mechanical wave propagation in a soft polymer film. A composite piezo actuator encapsulated in soft ecoflex polymer film was employed to generate the mechanical wave in a 0.5- to 7.0-kHz frequency range. The shear wave was propagating along the film. The surface vertical fluctuations at two different points, ~388 μm apart, were simultaneously monitored by two cantilevers engaged on the film surface. To minimize the influence on the viscoelastic properties of polymer induced by cantilevers, soft cantilevers with spring constants from 0.02 to 0.03 N/m were used (44). The schematic of the platform and the measured vibration amplitude spectrum are shown in Fig. 4 *A* and *B*, respectively. The amplitude of the

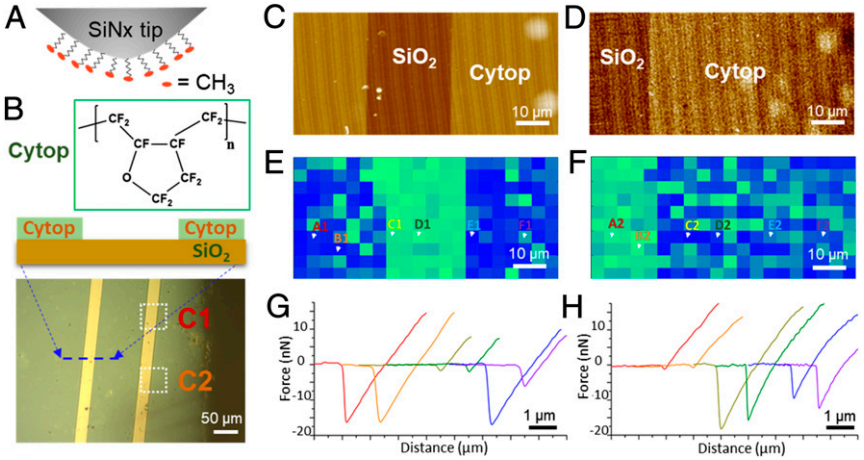

Fig. 3. Parallel structure-hydrophobicity mapping in water. (*A*) Schematic of OTS-functionalized hydrophobic AFM tip. (*B*) Schematic and optical images of the Cytop-SiO_2 sample. Insets (C1, C2) demonstrate areas imaged in *C* and *D*, respectively. (*C* and *D*) Parallel SEA-AFM morphology images. (*E* and *F*) Parallel adhesion maps of the areas in *C*, *D*, *G*, and *H*. Typical force-distance curves measured at the indicated locations in *E* and *F*.

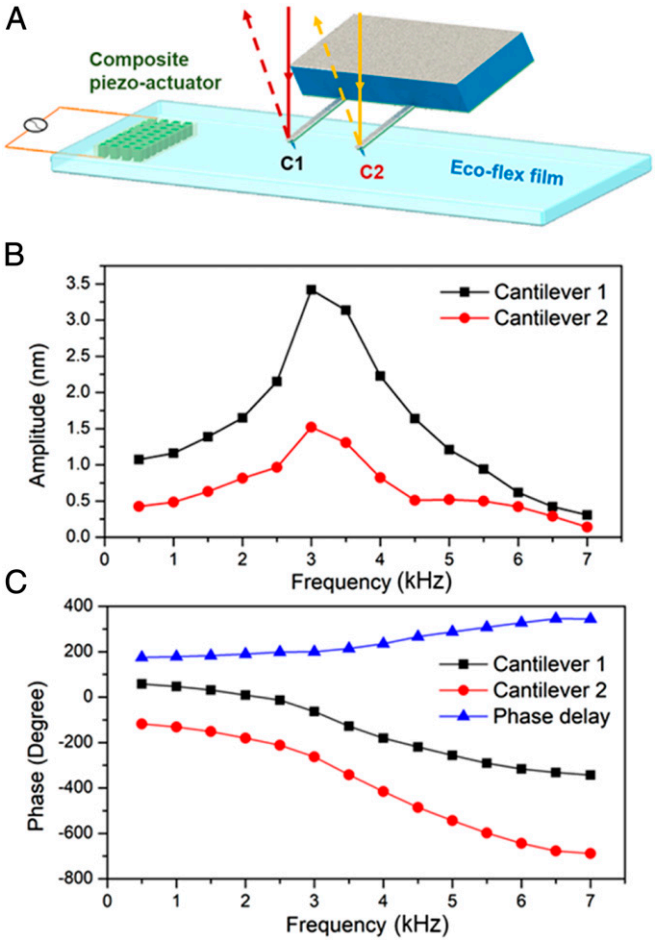

Fig. 4. Mechanical wave propagation sensing. (*A*) Schematic of the two-cantilever array AFM to detect the wave propagation in a piezoelectric actuator encapsulated in polymer film. The piezo actuator is driven by frequencies from 0.5 to 7.0 kHz. The array cantilevers detect the motion at the two points on the film surface simultaneously. (*B*) The frequency-dependent amplitude and (*C*) phases of cantilever 1 (black) and cantilever 2 (red). The blue curve in *C* represents the phase delay between the two probes.

propagating mechanical wave is ∼0.5 to 3.5 nm, with a resonance peak of the radial mode located at ∼3 kHz (45). The amplitude measured from cantilever 2 is smaller than that from cantilever 1, because cantilever 1 is located closer to the actuator and the wave energy is dampened during propagation (46). This is validated by monitoring the amplitude change while placing the same cantilever closer to the source (*SI Appendix*, Fig. S8). We resolved the frequency-dependent phase delay between the two probes (Fig. 4*C*, blue line), which is related to the wave propagation speed in the polymer. These results indicate that the parallel AFM could lead to reliable and flexible applications for detecting mechanical wave propagation along soft polymer films. With subnanometer resolution sensitivity, mechanical signatures from many systems, such as mechanical wave propagation during tissue expansions (47) and wave attenuation and retardation in materials characterization for defects inspection (48) are conveniently accessed by the array AFM and will benefit more investigations in future studies.

Intercellular Cooperative Activities. We explored the potential of the array SEA-AFM platform in detecting the coordinated activities of a dynamic biomechanical system. Initially, we placed two probes onto a monolayer of neonatal mouse cardiomyocytes (Fig. 5*A* shows optical images). The two morphology images of the fixed cells obtained by the two cantilevers in constant height mode are shown in Fig. 5*B*. Live cardiomyocyte monolayer enabled us to record cardiomyocyte contractions when uncoupled and coupled, shown in Fig. 5 *C* and *D*, respectively. With the two AFM cantilevers positioned on two separate cells, simultaneous localized contractile activities and dynamic morphological changes were examined by measuring transverse displacements.

Spontaneous activity from two separate cardiomyocytes (C1, red line and C2, black line) suggests that the two cells were uncoupled: compare the peak-to-peak distances and overlap between C1 and C2 in Fig. 5 *C*, *i* (dotted lines). In the pacing experiments of 1.8 Hz and 4 Hz, the localized contractile activities of the two cells (i.e., changes in cell height with active contraction) are illustrated in Fig. 5 *C*, *ii* and *iii*. Cell C1 was successfully paced at 4 Hz but C2 could not be paced. These experiments confirm that array AFM can be used to study changes in the contraction of multiple cells simultaneously.

We further utilized array AFM to detect changes in electrical coupling between coupled cardiomyocytes, as an example of multicellular integrated biological systems. For modulating the coupling between cells, we used heptanol, a gap junction blocker (Fig. 5*D*). Note the similar frequency and overlap of contraction suggesting the coupling between C1 and C2 (dotted lines, Fig. 5 *D*, *i*). Before adding heptanol, the spontaneous contraction frequency of the two cells was synchronous with a measured frequency of ∼1.8 Hz. After 15-min incubation with 1 mM heptanol, both cells stopped contracting due to the reported effect of gap junction blockers (49). After washing away the blocker, the two cells resumed spontaneous contraction but with reduced contractile response (amplitude reduced) and they became asynchronous. Although the pace of contraction was similar for the two cells, C2 displayed delayed contraction (Fig. 5 *D*, *iii*); the lack of synchronization suggests gap junction function had not yet returned to initial conditions.

These results demonstrate the biological applicability of the SEA-AFM system. This approach has several advantages over other methods currently in use in its ability to simultaneously measure micromechanical properties of two single cells with high spatial (submicron) and temporal (microsecond) resolution (24). Future experiments combining the detection of electrical signals (*SI Appendix*, section 3 and Fig. S9) with force propagation using multiprobe AFM would decipher essential novel mechanisms with respect to arrhythmogenic pathophysiology.

Conclusion

In summary, a SEA-AFM platform was developed to achieve simultaneous multipoint, multiscale structure–function analysis both in air and in liquid. The main advantage of the SEA-AFM over other existing array AFM is its ability to optically address closely packed probe–sample interaction signals without cross-talk or further complicating the system. We have demonstrated the versatility and robustness of the SEA-AFM system for multipoint morphology imaging, surface hydrophobicity, and electric potential mapping. In addition, taking advantage of its high sensitivity and biological compatibility, we recorded dynamic mechanical wave propagation in polymer film and intercellular activities of cardiomyocytes in real time. A number of innovative implementations can be envisioned from this array AFM platform, providing new perspectives in a wide range of fields, including multipoint manipulations/fabrications, multifunctional sensing, and robotic cantilever arrays.

Methods

Array AFM Setup. The array AFM system is adapted from a MultiMode AFM (Bruker) with Nanoscope III controller by customizing both illumination and deflection beam paths. A supercontinuum laser (Extreme; NKT Photonics. Inc.) is used to illuminate cantilever arrays through a dispersive grating and an objective lens. The AFM head is customized to have a top opening for illumination and side opening for deflection beam detection. Two QPDs (Skyhunt)

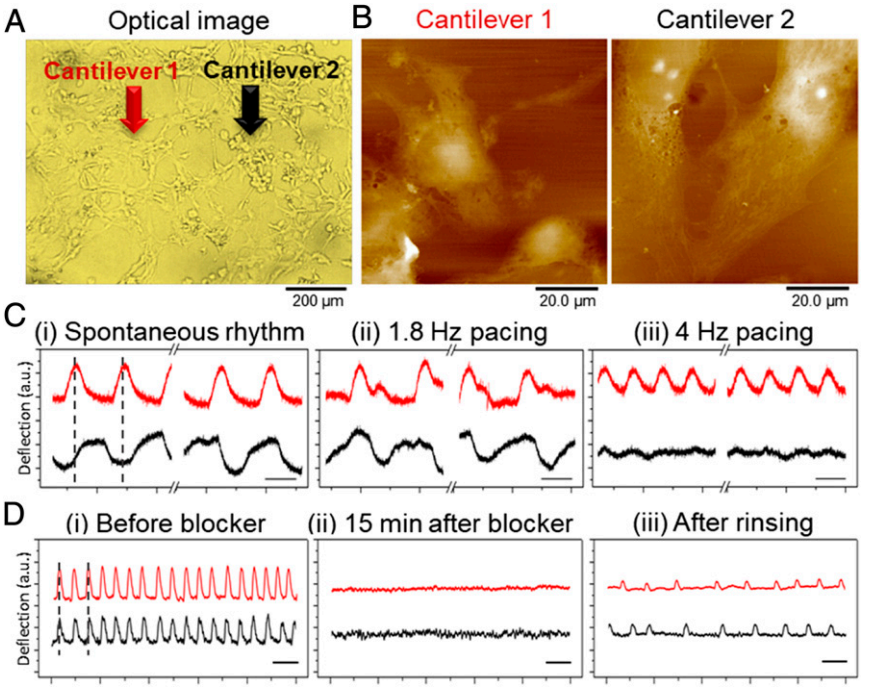

Fig. 5. Cardiomyocyte coordinated activity detection with SEA-AFM. (*A*) Optical image of live neonatal mouse cardiomyocytes acquired using the optical microscope equipped on the SEA-AFM system. (*B*) Morphology images from dual SEA-AFM tips of fixed cardiomyocytes in liquid. (*C*) Simultaneous detection of localized contractile activity of two beating cardiomyocytes (C1, red line and C2, black line) during (*i*) spontaneous beating and pacing at rates of (*ii*) 1.8 Hz and (*iii*) 4 Hz. (Scale bars: 250 ms.) (*D*) The gap junction uncoupler heptanol (1 mM) prevents cell-to-cell electrotonic conduction. Output of the photodetector of cantilever 1 (red) and cantilever 2 (black) (*i*) before and (*ii*) 15 min after the blocker was applied and (*iii*) 5 min after the blocker was washed away. (Scale bars: 1 s.)

are used to monitor the deflected beams from two cantilevers, respectively. The two deflected beams are separated by a dichroic mirror (Semrock). Two programmable amplifiers (Alligator Technologies)/locking-in amplifiers (SR830 DSP; Stanford Research Systems) amplify the signal from QPDs and send it to AFM through a Signal Access Module. The system is operated with passive cantilever array, and all of the AFM images are taken in constant height mode. In our current complementation, the supercontinuum laser was operated with around 300-ps pulse duration at 78-MHz repetition frequency. The peak power was around 40 times the average power. Considering the comparatively high peak energy and large laser spot size, special attention has to be paid when imaging photosensitive specimens, and the laser power, pulse duration, and wavelength range should be adjusted accordingly (50, 51).

Array AFM for the Hydrophobicity Mapping. We measured the adhesive forces between the chemically functionalized probes and the patterned sample surface using a modified method published previously (42). The parallel AFM force measurements from two cantilevers were carried out simultaneously in deionized water by using a fluid cell (Bruker). The force-displacement curves were performed at a scan rate of 1 Hz and a z-velocity of 8 μm/s, recorded over an array of points (20 × 10 pixels in step size of 4 μm). The magnitude of the pull-off peaks occurring upon retraction of the probes was analyzed. The force curve data were postprocessed with Python.

Array AFM Setup for the Measurement of Mechanical Wave Propagation on Soft Polymer Film. The 1–3 piezo composite material (Smart Material) of size 1.8 × 1.8 mm and thickness 200 μm was encapsulated in a soft ecoflex (ecoflex 00-30; Smooth-On, Inc.) polymer film. The actuator is sinusoidally excited by a function generator (DSO1012A; Agilent Technologies) (10-V amplitude, 0.5 to 7.0 kHz). The film surface vertical fluctuation at two different points with a distance of ∼388 μm were simultaneously monitored by the parallel cantilever array system. To further improve the signal-to-noise ratio, the output of the QPD was processed by two lock-in amplifiers (SR830 DSP; Stanford Research Systems) using the driving signal of the piezo-actuator as a reference.

Array AFM Setup for the Detection of Cardiomyocyte Coordinated Activities. The cell samples on the glass slides were mounted on the AFM sample holder and loaded into the liquid cell. An illumination and detection setup similar to that in the wave propagation experiment was used to detect the cardiomyocyte contractile activities. The output of the QPDs was recorded using a National Instruments DAQ with a custom LabView 8.0 program. Sample rate was 1,000 Hz, and the filter cutoff was 100 Hz. To minimize the damage to the cells, we used soft AFM cantilevers with a spring constant in the range of 0.02 to 0.03 N/m. In the pacing experiments, the monolayered cardiomyocytes were paced with a pair of platinum electrodes with a 12-ms, 85-V pulse using an SD9 stimulator (Grass Technologies) at two pacing rates, 1.8 Hz and 4 Hz. The electrode wires were applied to the system via two channels of the AFM liquid cell. All use of experimental animals was performed according to animal use protocol (#S01013M) approved by the University of California, San Diego Institutional Animal Care and Use Committee. All use of human induced pluripotent stem cells was approved by the University of California, San Diego Human Research Protections Program and Institutional Review Board/The Embryonic Stem Cell Research Oversight Committee for project 161206ZX.

ACKNOWLEDGMENTS. We thank Shuai Lou, Abhijith Karkisaval, Dr. Eric Huang, Juan Ybarra, Dr. Xuekun Lu, Dr. Pillip Kyriakakis, and Dr. Michael Todd for helpful discussion and Somok Mondal, Haowei Jiang, and Dr. Drew Hall for their support in noise spectra density measurement and analysis. This work was supported by National Institute on Aging of National Institutes of Health Grant AG028709 (to R.L.), NIH Grant 1 R01 HL137100 (to A.D.M.), Veteran Affairs Merit Award BX003671 from the Department of Veterans Affairs (to B.P.H.), and the Gordon and Betty Moore Foundation Grant 4827 to (to F.A.). This work was performed in part at the San Diego Nanotechnology Infrastructure (SDNI) of University of California, San Diego (UCSD), a member of the National Nanotechnology Coordinated Infrastructure (NNCI), which is supported by the National Science Foundation (Grant ECCS-1542148). We also acknowledge the UCSD Jacob School of Engineering Center for Wearable Sensors.

1. Mann S (2009) Self-assembly and transformation of hybrid nano-objects and nanostructures under equilibrium and non-equilibrium conditions. *Nat Mater* 8:781–792.
2. Soumyanarayanan A, Reyren N, Fert A, Panagopoulos C (2016) Emergent phenomena induced by spin-orbit coupling at surfaces and interfaces. *Nature* 539:509–517.
3. Buzsáki G (2004) Large-scale recording of neuronal ensembles. *Nat Neurosci* 7: 446–451.
4. Biele R, Rodríguez-Rosario CA, Frauenheim T, Rubio A (2017) Controlling heat and particle currents in nanodevices by quantum observation. *npj Quantum Mater* 2:38.

5. Spira ME, Hai A (2013) Multi-electrode array technologies for neuroscience and cardiology. *Nat Nanotechnol* 8:83–94.
6. Shafique E, et al. (2013) Genetically encoded fluorescent indicator for intracellular hydrogen peroxide. *Nat Methods* 5:515–530.
7. Weissleder R (2002) Scaling down imaging: Molecular mapping of cancer in mice. *Nat Rev Cancer* 2:11–18.
8. Ogawa S, Lee TM, Kay AR, Tank DW (1990) Brain magnetic resonance imaging with contrast dependent on blood oxygenation. *Proc Natl Acad Sci USA* 87:9868–9872.
9. Ross FM (2015) Opportunities and challenges in liquid cell electron microscopy. *Science* 350:aaa9886.
10. Lal R, John SA, Laird DW, Arnsdorf MF (1995) Heart gap junction preparations reveal hemiplaques by atomic force microscopy. *Am J Physiol* 268:C968–C977.
11. Lal R, Yu L (1993) Atomic force microscopy of cloned nicotinic acetylcholine receptor expressed in Xenopus oocytes. *Proc Natl Acad Sci USA* 90:7280–7284.
12. Tortonese M, Barrett RC, Quate CF, Tortonese M (1993) Atomic resolution with an atomic force microscope using piezoresistive detection atomic resolution with an atomic force microscope piezoresistive detection. *Appl Phys Lett* 62:834–836.
13. Müller DJ, Dufrêne YF (2008) Atomic force microscopy as a multifunctional molecular toolbox in nanobiotechnology. *Nat Nanotechnol* 3:261–269.
14. Cui L, et al. (2018) Peltier cooling in molecular junctions. *Nat Nanotechnol* 13:122–127.
15. Alsteens D, et al. (2015) Imaging G protein-coupled receptors while quantifying their ligand-binding free-energy landscape. *Nat Methods* 12:845–851.
16. Ionescu-Zanetti C, Mechler A, Carter SA, Lal R (2004) Semiconductive polymer blends: Correlating structure with transport properties at the nanoscale. *Adv Mater* 16: 385–389.
17. Puntes VF, Gorostiza P, Aruguete DM, Bastus NG, Alivisatos AP (2004) Collective behaviour in two-dimensional cobalt nanoparticle assemblies observed by magnetic force microscopy. *Nat Mater* 3:263–268.
18. Alsteens D, et al. (2017) Atomic force microscopy-based characterization and design of biointerfaces. *Nat Rev Mater* 2:17008.
19. Shan Y, Wang H (2015) The structure and function of cell membranes examined by atomic force microscopy and single-molecule force spectroscopy. *Chem Soc Rev* 44: 3617–3638.
20. Putman CAJ, et al. (1998) A detailed analysis of the optical beam deflection technique for use in atomic force microscopy. *J Appl Phys* 72:6–12.
21. Fritz J, et al. (2000) Translating biomolecular recognition into nanomechanics. *Science* 288:316–318.
22. Lang HP, et al. (1998) Sequential position readout from arrays of micromechanical cantilever sensors. *Appl Phys Lett* 72:383–385.
23. Somnath S, Kim HJ, Hu H, King WP (2014) Parallel nanoimaging and nanolithography using a heated microcantilever array. *Nanotechnology* 25:014001–014012.
24. Shroff SG, Saner DR, Lal R (1995) Dynamic micromechanical properties of cultured rat atrial myocytes measured by atomic force microscopy. *Am J Physiol* 269:C286–C292.
25. Koelmans WW, et al. (2010) Parallel optical readout of cantilever arrays in dynamic mode. *Nanotechnology* 21:395503.
26. Sulchek T, et al. (2001) Parallel atomic force microscopy with optical interferometric detection. *Appl Phys Lett* 78:1787.
27. Kim SJ, Ono T, Esashi M (2006) Capacitive resonant mass sensor with frequency demodulation detection based on resonant circuit. *Appl Phys Lett* 88:1–3.
28. Rogers B, Manning L, Sulchek T, Adams JD (2004) Improving tapping mode atomic force microscopy with piezoelectric cantilevers. *Ultramicroscopy* 100:267–276.
29. Dukic M, et al. (2016) Direct-write nanoscale printing of nanogranular tunnelling strain sensors for sub-micrometre cantilevers. *Nat Commun* 7:12487.
30. Ivaldi P, et al. (2011) 50 nm thick AlN film-based piezoelectric cantilevers for gravimetric detection. *J Micromech Microeng* 21:085023.
31. Shekhawat G, Tark SH, Dravid VP (2006) MOSFET-Embedded microcantilevers for measuring deflection in biomolecular sensors. *Science* 311:1592–1595.
32. Despont M, et al. (2000) VLSI-NEMS chip for parallel AFM data storage. *Sens Actuators A Phys* 80:100–107.
33. Kim HJ, Dai Z, King WP (2013) Thermal crosstalk in heated microcantilever arrays. *J Micromech Microeng* 23:025001.
34. Rangelow IW, et al. (2017) Review article: Active scanning probes: A versatile toolkit for fast imaging and emerging nanofabrication. *J Vac Sci Technol B Nanotechnol Microelectron Mater Process Meas Phenom* 35:06G101.
35. Fukuma T, Kimura M, Kobayashi K, Matsushige K, Yamada H (2005) Development of low noise cantilever deflection sensor for multienvironment frequency-modulation atomic force microscopy. *Rev Sci Instrum* 76:053704.
36. Walters DA, et al. (1996) Short cantilevers for atomic force microscopy. *Rev Sci Instrum* 67:3583–3590.
37. Schumacher Z, Miyahara Y, Aeschimann L, Grütter P (2015) Improved atomic force microscopy cantilever performance by partial reflective coating. *Beilstein J Nanotechnol* 6:1450–1456.
38. Fukuma T, Jarvis SP (2006) Development of liquid-environment frequency modulation atomic force microscope with low noise deflection sensor for cantilevers of various dimensions. *Rev Sci Instrum* 77:1–8.
39. Fukuma T (2009) Wideband low-noise optical beam deflection sensor with photothermal excitation for liquid-environment atomic force microscopy. *Rev Sci Instrum* 80:023707.
40. Schäffer TE, Hansma PK (1998) Characterization and optimization of the detection sensitivity of an atomic force microscope for small cantilevers. *J Appl Phys* 84: 4661–4666.
41. Minne SC, Manalis SR, Quate CF (1995) Parallel atomic force microscopy using cantilevers with integrated piezoresistive sensors and integrated piezoelectric actuators. *Appl Phys Lett* 67:3918.
42. Munz M, Giusca CE, Myers-Ward RL, Gaskill DK, Kazakova O (2015) Thickness-dependent hydrophobicity of epitaxial graphene. *ACS Nano* 9:8401–8411.
43. Bongiovanni MN, et al. (2016) Multi-dimensional super-resolution imaging enables surface hydrophobicity mapping. *Nat Commun* 7:13544.
44. Amirkhizi AV, Isaacs J, McGee J, Nemat-Nasser S (2006) An experimentally-based viscoelastic constitutive model for polyurea, including pressure and temperature effects. *Philos Mag* 86:5847–5866.
45. Certon D, Casula O, Patat F, Royer D (1997) Theoretical and experimental investigations of lateral modes in 1-3 piezocomposites. *IEEE Trans Ultrason Ferroelectr Freq Control* 44:643–651.
46. Definitions BV, Sperling LH (1990) *Sound and Vibration Damping with Polymers Basic Viscoelastic Definitions and Concepts* (American Chemical Society, Washington, DC).
47. Serra-Picamal X, et al. (2012) Mechanical waves during tissue expansion. *Nat Phys* 8: 628–634.
48. Kazemirad S, Mongeau L (2013) Rayleigh wave propagation method for the characterization of a thin layer of biomaterials. *J Acoust Soc Am* 133:4332–4342.
49. Keevil VL, Huang CL, Chau PL, Sayeed RA, Vandenberg JI (2000) The effect of heptanol on the electrical and contractile function of the isolated, perfused rabbit heart. *Pflugers Arch* 440:275–282.
50. Xu C, Wise FW (2013) Recent advances in fibre lasers for nonlinear microscopy. *Nat Photonics* 7:875–882.
51. Latina MA, Park C (1995) Selective targeting of trabecular meshwork cells: In vitro studies of pulsed and CW laser interactions. *Exp Eye Res* 60:359–371.